Small

www.small-journal.com

Wafer-Scale Self-Limiting Epitaxy of Bernal-Stacked Single-Crystal Boron Nitride

Jaewon Wang[1] | Hyeonwoo Lee[1] | Jaemin Kim[2] | Haeng Un Yeo[1] | Cheol Hwan Yoon[1] | Min Seok Yoo[3] | Junseop Noh[1] | Sora Jang[1] | Ju-Hyoung Han[1] | Juwon Han[1] | Jaeeun Park[1] | Young Ho Jin[1] | Huijun Han[1] | Kitae Park[1] | Joonki Suh[1] | Tae-Sik Yoon[1] | Seunguk Song[4,5] | Minsu Seol[3] | Chanyong Hwang[6] | Hyung-Joon Shin[1] | Zonghoon Lee[2] | Changwook Jeong[1] | Soon-Yong Kwon[1]

[1]Department of Materials Science and Engineering and Graduate School of Semiconductor Materials and Devices Engineering, Ulsan National Institute of Science and Technology (UNIST), Ulsan, Republic of Korea | [2]Center for Multidimensional Carbon Materials (CMCM), Institute for Basic Science (IBS), Ulsan, Republic of Korea | [3]2D Device Laboratory, Samsung Advanced Institute of Technology (SAIT), Suwon, Republic of Korea | [4]Department of Energy Science, Sungkyunkwan University (SKKU), Suwon, Republic of Korea | [5]Center for 2D Quantum Heterostructures (2DQH), Institute for Basic Science (IBS), Suwon, Republic of Korea | [6]Quantum Technology Institute, Korea Research Institute of Standards and Science (KRISS), Daejeon, Republic of Korea

Correspondence: Hyung-Joon Shin (shinhj@unist.ac.kr) | Zonghoon Lee (zhlee@unist.ac.kr) | Changwook Jeong (changwook.jeong@unist.ac.kr) | Soon-Yong Kwon (sykwon@unist.ac.kr)

Received: 31 October 2025 | **Revised:** 5 March 2026 | **Accepted:** 5 March 2026

Keywords: 2D dielectric integration | Bernal-stacked boron nitride (bBN) | metastable epitaxy | self-limiting growth | step-edge engineering | wafer-scale growth

ABSTRACT

Non-centrosymmetric stacking in boron nitride (BN) enables out-of-plane polarization, offering a route toward 2D dielectrics with embedded nonvolatile functionality. However, achieving uniform, wafer-scale growth of metastable Bernal-stacked BN (bBN) remains challenging, as it requires breaking interlayer inversion symmetry. Here, we demonstrate the wafer-scale epitaxial growth of single-crystal bBN bilayers on Ni(111)/sapphire substrates using metal-organic chemical vapor deposition. By employing a flow-modulation epitaxy approach, we enhanced surface reaction kinetics while suppressing secondary nucleation, thereby enabling self-limiting growth of uniform bilayer bBN films. Monoatomic Ni step edges deterministically enforced the AB stacking order, energetically stabilizing the bilayer configuration by lifting the degeneracy of competing stacking orientations, as confirmed by atomic-resolution imaging and density functional theory calculations. The resulting bBN films served as atomically thin dielectric interlayers in top-gated molybdenum disulfide (MoS_2) transistor arrays, yielding spatially uniform device performance across the wafer and enabling nonvolatile ferroelectric switching of the MoS_2 channels via polarization reversal in the bBN interlayer. These results expand the understanding of step-edge-guided growth mechanisms for controlling stacking order and layer number in metastable 2D materials, and demonstrate a reliable wafer-scale approach to phase-controlled synthesis of single-crystal bBN bilayers with their integration as functional 2D dielectrics for practical electronic applications.

1 | Introduction

The phase-dependent stacking order of 2D layered materials plays a pivotal role in defining their (opto)electronic structure, interlayer coupling, and symmetry-governed physical properties [1–3]. For instance, hexagonal boron nitride (hBN) typically adopts the thermodynamically stable AA′ stacking, and has been extensively used as a dielectric support or encapsulation layer in van der Waals (vdW) heterostructures due to its atomically flat, chemically inert surface and large bandgap [4–9]. Beyond the conventional AA' stacking, however, metastable, non-centrosymmetric configurations—such as Bernal (AB) and

This is an open access article under the terms of the Creative Commons Attribution-NonCommercial License, which permits use, distribution and reproduction in any medium, provided the original work is properly cited and is not used for commercial purposes.

© 2026 The Author(s). *Small* published by Wiley-VCH GmbH

rhombohedral (ABC) stacking in BN crystals—have attracted growing interest due to their fundamentally distinct interlayer symmetry and emergent features, including sliding ferroelectricity and optical nonlinearity [10–14]. Notably, Bernal-stacked BN (bBN) offers fundamentally distinct features—including enhanced stacking registry with 2D materials, flat-band formation in Moiré superlattices, and direct-gap behavior—thereby broadening its applicability to emerging 2D (opto)electronic devices [15–20].

Meanwhile, the demand for wafer-scale single-crystal BN has surged to support large-area 2D integration platforms [7]. Most growth strategies have focused on (111)-oriented single-crystal metals such as Cu, Ni, Cu–Ni, and Ni–Fe alloys, which offer favorable lattice matching with BN [11, 21–25]. Despite the inherent C_{6v} symmetry of these surfaces, the presence of <110> step edges breaks the rotational symmetry, enabling unidirectional domain alignment via step-edge-guided growth [26]. This approach has proven effective in both monolayer and multilayer regimes. However, synthesized multilayer BN films often exhibit diverse stacking sequences—including AA', AB, and ABC stacking configurations—highlighting that the role of step edges in controlling stacking order during nucleation is still not fully understood [11, 22]. In addition, BN exhibits strong layer-dependent physical properties, such as reduced tunneling and enhanced dielectric screening with increasing thickness, particularly beyond the bilayer regime [27, 28]. Moreover, in the case of bBN, precise layer control is essential to ensure uniform ferroelectric properties, as internal polarization can be cancelled depending on the number of layers [29].

Previous approaches using single-crystal Ni substrates yielded multilayer BN with varying thicknesses depending on precursor flow and growth time, indicating the absence of any self-limiting bilayer growth behavior [10, 22]. Despite proceeding under a surface-mediated growth regime, the use of single-source precursors, such as borazine or ammonia borane [21–23, 30–37], hindered independent control over the kinetics of B and N surface reactions, thereby impeding the reliable formation of a consistent layer number. As such, self-limiting growth has only been achieved for monolayer hBN on Cu substrates, which exhibits low solubility for both elements, and the scalable realization of uniform bilayer BN with defined stacking order remains a fundamental challenge (Table S1).

In this study, we report the wafer-scale, self-limiting epitaxial growth of Bernal-stacked bilayer single-crystal BN on Ni(111)/sapphire substrates using a flow-modulated metal-organic chemical vapor deposition (MOCVD) technique. By leveraging the crystallographic guidance of monoatomic Ni step edges, we achieved not only unidirectional domain alignment but also deterministic AB stacking order with uniform bilayer thickness control. Remarkably, the bilayer nucleation exhibited self-limiting behavior across the entire wafer, remaining strictly two layers thick independent of precursor flux. The resulting bBN films were integrated as atomically thin dielectric interlayers in top-gated molybdenum disulfide (MoS_2) transistors, yielding spatially uniform electronic performance across large-area device arrays and enabling threshold voltage modulation of the MoS_2 channel via ferroelectric polarization switching in the bBN layer. These findings establish a generalizable strategy for stacking-controlled growth of 2D materials, providing wafer-scale access to metastable bBN and demonstrating its scalable integration as a functional dielectric in practical 2D electronic applications.

2 | Results and Discussion

2.1 | Self-Limiting Bilayer Growth of bBN Films via Flow-Modulation Epitaxy

A bilayer bBN film was synthesized using a vertical showerhead-type cold-wall MOCVD system equipped with run/vent manifold switching, enabling the sequential feeding of precise amounts of precursors. The film was grown on a single-crystal Ni(111) thin film deposited on a two-inch c-plane sapphire substrate. To independently regulate the injection of B and N sources during bBN synthesis, triethyl-boron (TEB) and ammonia (NH_3) were used, with hydrogen (H_2) as carrier gas. The growth temperature was set to 1100 °C, which provided optimal conditions for lateral growth of bBN domains, while preventing Ni decomposition (Figure S1).

When two different precursors coexist at high partial pressures, gas-phase nucleation and parasitic reactions—both typical in MOCVD systems—can occur [38–40]. In continuous-flow MOCVD, the high N/B ratio results in a dominant partial pressure of NH_3 on the Ni(111) surface, which suppresses the B–N reaction rate [41], thereby reducing the overall growth rate of bBN (Figure 1a,b). In contrast, under flow-modulation epitaxy conditions (Figure 1c), where the precursors are injected sequentially, the bBN surface coverage reached 99%, with the adlayer fraction saturating at ~4% of the total bBN area (Figure 1d; Figure S2). This result was achieved under identical TEB injection durations (20 min) by regulating the partial pressure of precursors on the Ni(111) surface, thereby enhancing the B—N reaction rate. A complete bBN film was formed on the Ni(111) surface within 67 min, corresponding to 200 precursor pulse cycles. Secondary nucleation was effectively suppressed by optimizing the interruption interval between precursor feeds (Figure S3). However, when this interval exceeded the optimal range, bBN coverage decreased due to the desorption of residual precursors from the surface.

In flow-modulation epitaxy of bBN on Ni(111), achieving wafer-scale uniformity requires consistent nucleation thickness and comparable nucleation behavior across spatially distinct regions. Under the 50-pulse-cycle condition, where bBN domains had not yet fully coalesced, uniform trends in both domain size and surface coverage were observed (Figure S4). To examine whether bBN domains exhibit consistent thickness during heterogeneous nucleation, a bBN film grown for 100 pulse cycles was transferred and subsequently analyzed (Figure 1f–h; Figure S5). The measured thickness was approximately 0.83 nm on average, confirming that bilayer nucleation dominated irrespective of the measurement position. When a large number of TEB injections were applied within the optimum interval, the B–N reaction rate decreased, reducing bBN coverage (Figure S6a–c). However, under these same conditions, the thickness of the transferred bBN films (Figure S6d,e) remained constant (Figure 1h), even with increased B-source dosing, indicating that the bBN growth process follows a self-limiting mechanism under the designed

16136829, 0, Downloaded from https://onlinelibrary.wiley.com/doi/10.1002/smll.202513245 by Ulsan National Institute Of, Wiley Online Library on [02/04/2026]. See the Terms and Conditions (https://onlinelibrary.wiley.com/terms-and-conditions) on Wiley Online Library for rules of use; OA articles are governed by the applicable Creative Commons License

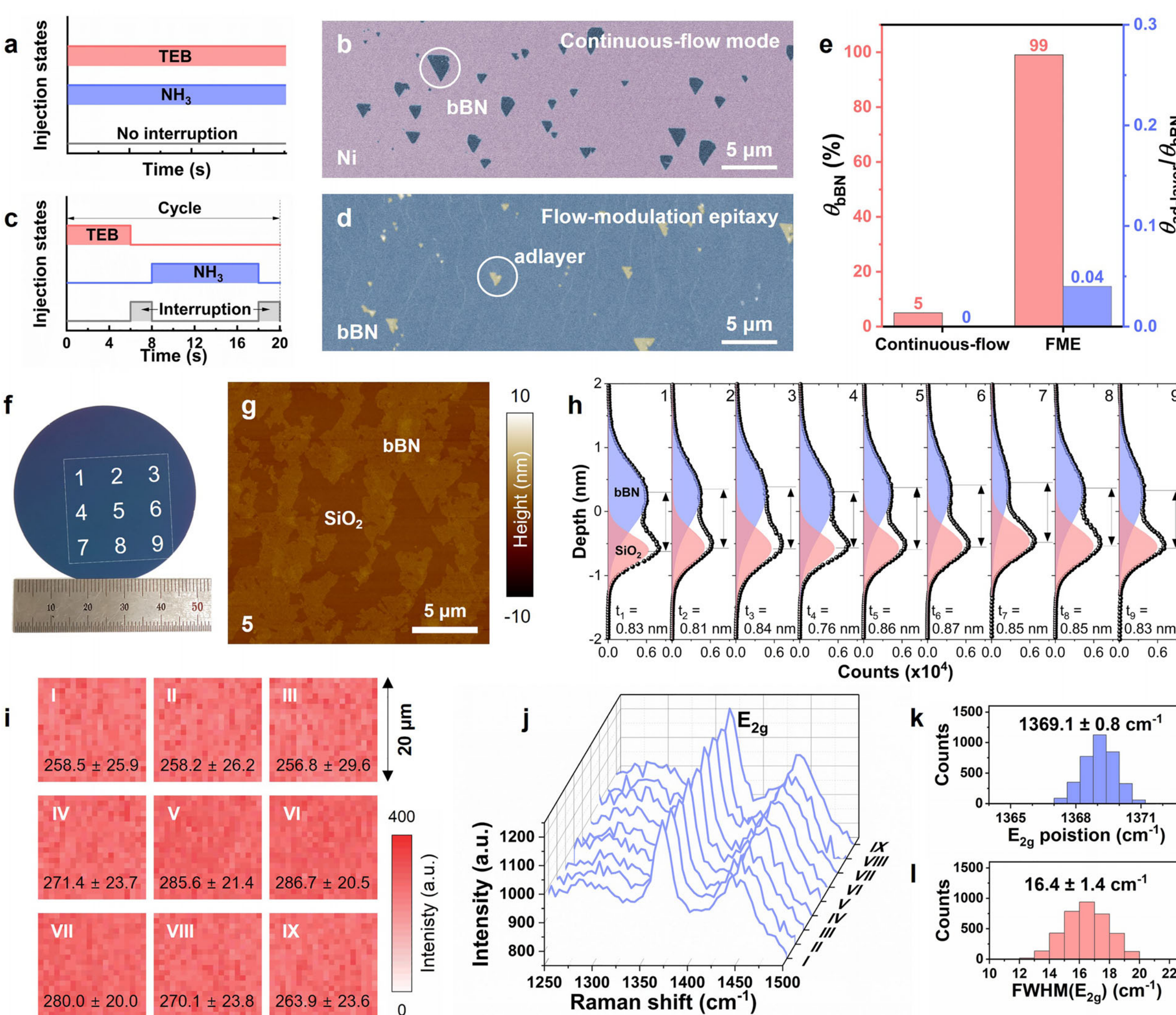

FIGURE 1 | Growth and characterization of uniform bilayer bBN films. a–d) Schematics of precursor injection states (a, c) and corresponding false-colored SEM images (b, d) under continuous-flow mode (a) and flow-modulation epitaxy (c). e) Surface coverage of bBN (θ_{bBN}) and adlayer-to-bBN coverage ratio (θ_{adlayer} /θ_{bBN}) extracted from the growth modes shown in (a) and (c). (f) Photograph of partially grown bBN film (100 pulse cycles) transferred onto a two-inch SiO_2/Si wafer, showing nine designated AFM measurement positions. (g) AFM image at position 5 in (f), displaying bBN domains on the SiO_2 surface. (h) Depth profiles extracted from the nine positions in (f). Two Gaussian distributions, corresponding to the bBN layer (sky blue) and SiO_2 substrate (pink), were fitted to the depth histograms. The bBN thickness (t_1–t_9) was determined from the difference in the peak centers. (i) Raman intensity maps of the E_{2g} phonon mode from nine regions marked in Figure S10, with average intensity values included. (j) Representative Raman spectra from each region shown in (i). (k, l) Distributions of E_{2g} peak positions (k) and FWHM (l).

flow-modulation conditions. To probe the effect of excessive B-source dosing on subsequent BN growth, TEB was pre-dosed for one minute prior to the standard 200 pulse cycles. When no interval was introduced between the pre-dose and the pulse cycles, bBN did not grow (Figure S7). In contrast, introducing a one-minute interval increased bBN coverage to 90% (Figure S8). These results indicate that the growth is governed by a surface-reaction mechanism [42], where maintaining an optimal B:N ratio at the surface is more critical for bBN formation than the absolute precursor supply (Figure S9; see Note S1 for details).

Transfer of the two-inch bBN film was achieved through the electrochemical bubbling method (Figure S10) [21, 34, 43]. Raman mapping and optical contrast analysis confirmed the film's uniformity over a large area (Figure 1i–l; Figure S11). The E_{2g} phonon mode intensity exhibited minimal spatial variation, with an average of 270.1 ± 26.4 cm^{-1}. The peak position closely matched that of mechanically exfoliated bilayer hBN [44], and the full width at half maximum (FWHM) of 16.4 ± 1.4 cm^{-1} indicated a crystal quality comparable to that of previously reported CVD-grown single-crystal hBN films [21, 22]. Furthermore, the fully merged bBN film—despite minor adlayer coverage and edge tearing induced during bubbling transfer—exhibited a thickness consistent with that of the partially grown bBN film (Figures S12 and S13).

Ultraviolet-visible (UV–vis) absorption spectroscopy and X-ray photoelectron spectroscopy (XPS) revealed key characteristics of the bBN film. The film exhibited an optical band gap of approximately 6.0 eV (Figure S14) and was composed of sp^2-hybridized

16136829, 0, Downloaded from https://onlinelibrary.wiley.com/doi/10.1002/smll.202513245 by Ulsan National Institute Of, Wiley Online Library on [02/04/2026]. See the Terms and Conditions (https://onlinelibrary.wiley.com/terms-and-conditions) on Wiley Online Library for rules of use; OA articles are governed by the applicable Creative Commons License

B—N bonding (Figure S15). The [B]:[N] ratio, determined for the bBN film transferred onto a SiO_2/Si wafer, was found to be 1.00:0.98 based on the B *1s* (190.4 eV) and N *1s* (398.1 eV) core-level spectra. Conductive atomic force microscopy (CAFM) was used to evaluate the defect density and homogeneity of the as-grown bilayer bBN films on Ni(111) [45–47]. Because of the sub-1-nm thickness of bilayer bBN, tunneling currents are expected in the presence of structural defects such as pinholes and grain boundaries (GBs) [45]. However, current mapping revealed no measurable current, confirming the insulating nature and high structural integrity of the as-grown bBN films (Figures S16–S18). In addition, statistical analysis of 25 randomly acquired *I–V* curves showed uniform tunneling behavior (Figure S19), consistent with previous observations in CVD-grown single-crystal BN [47].

2.2 | Epitaxial Growth of Single-Crystal bBN on Ni(111)

Achieving a single-crystalline Ni(111) film with uniform step edges is a crucial prerequisite for guiding the unidirectional nucleation of bBN. To this end, we prepared single-crystal Ni(111) thin films on *c*-plane sapphire substrates by controlling the surface termination of sapphire (Figure S20) and performing H_2 annealing (see Experimental Section for details). The as-deposited Ni film exhibited a (111) crystallographic orientation along the nominal out-of-plane direction (Figure S21), while a twin GB was observed in the in-plane direction (Figure S22a–c). The H_2 annealing process facilitated atomic rearrangement, resulting in the formation of distinct stacking sequences and promoting abnormal grain growth [24, 25, 48, 49]. The annealed Ni film exhibited a single-crystal structure characterized by an atomically smooth, GB-free surface with well-defined <110> steps (Figure 2a; Figure S22b,d). Electron backscatter diffraction (EBSD) results (Figure 2b) confirmed that the Ni films maintained the (111) orientation and exhibited unidirectional in-plane alignment after bBN growth, with no evidence of mixed phases. This was further supported by the absence of Ni—B bond signals (~187.9 eV (ref. [22])) in the XPS spectra of the as-grown bBN film (Figure S15c). Scanning transmission electron microscopy (STEM) analysis confirmed the Ni/Al_2O_3 interface and revealed an in-plane epitaxial relationship of $[11\bar{2}]$Ni || [110]Al_2O_3 (Figure 2c,d).

The bBN domains were aligned with the underlying Ni step edges over a large area, as indicated by the white dashed lines in SEM and AFM phase images (Figure 2e,f). Following H_2 etching or UV/ozone (UVO) treatment, no alterations were observed in the merged bBN domain regions (e.g. BN partial etching or NiO_x formation), confirming the absence of GBs at the macroscale (Figures S23–S25) [35]. At the atomic scale, when two adjacent bBN domains merged, their congruent crystal orientations within both the individual domains and the merged region confirmed their seamless stitching (Figure S26). Integrated differential phase contrast (iDPC)-STEM was employed to confirm the bBN/Ni(111) interface configuration along both the zigzag and armchair directions of bBN (Figure 2g,h; Figure S27). Figure 2g shows that the lattice spacing of both $[11\bar{2}0]_{BN}$ and $[1\bar{1}0]_{Ni}$ is well-matched at 1.25 Å, with no observable mismatch. The atomic registry at the bBN/Ni interface was verified from a zigzag-view STEM image (Figure 2h). To assess the large-area crystal orientation of the as-grown bBN films, low-energy electron diffraction (LEED) measurements were performed at 16 different locations (Figure 2i). The resulting diffraction patterns exhibit six hexagonal spots with three-fold symmetry, consistently aligned across the scanned region, indicating a unidirectional crystal orientation of bBN.

2.3 | Step-Guided Uniform Nucleation of Bilayer bBN

We investigated the interface between bBN and Ni(111) at step edges using atomically resolved scanning tunneling microscopy (STM) to confirm the epitaxial relationship between the Ni steps and bBN. Large-area STM imaging revealed that the Ni(111) surface after bBN growth consisted of monoatomic steps and terraces (Figure 3a,b). As shown in Figure 3c, the STM image of the bBN grown along the Ni steps revealed a clear parallel alignment between the Ni < 110 > step direction and the zigzag direction of bBN. Fast Fourier transformation (FFT) analysis (inset of Figure 3c) further confirmed that the bBN lattice above and below the step maintained a consistent crystal orientation. The electrical bandgap of bBN was measured on both the upper and lower terraces using scanning tunneling spectroscopy (STS), yielding values of ~6 eV for both regions (Figure S28), consistent with the theoretical value [50]. This contrasts with monolayer hBN directly grown on metals, where hybridization with the substrate typically results in a reduced bandgap (<6 eV) [51, 52].

As shown in Figure 2h, bilayer bBN grown on Ni(111) adopts an AB stacking order. Because inversion symmetry is broken, bBN exhibits intrinsic polarization, with polarity reversed depending on the stacking sequence (AB or BA) [14]. A phase transition in the as-grown bBN/Ni films was confirmed by piezoresponse force microscopy (PFM), which demonstrated ferroelectric switching (Figure 3d). To verify that this stacking sequence persists beyond local regions, high-resolution TEM and SAED analyses were performed on transferred bBN films (Figure 3e–h; Figures S29 and S30). The atomic-resolution TEM image (Figure 3f) matched well with simulated images based on an AB-stacked BN model. A characteristic feature of AB stacking—the increased intensity of second-order diffraction spots relative to the first-order—was consistently observed [53, 54]. This diffraction signature was detected in both partially grown domains (Figure 3g,h) and fully merged films (Figure S29). Furthermore, electron beam-induced etching of the partially grown films (Figure S30) revealed triangular etch pits in the first and second layers with identical orientation, providing further confirmation of AB stacking, consistent with previous reports [53, 54].

To elucidate the thermodynamic origin of this stacking behavior, we combined density functional theory (DFT) calculations with structural characterization. Bilayer bBN was found to be energetically stabilized when nucleated at monoatomic Ni step edges. Two favorable configurations were identified: one with a B-terminated bBN edge and one with an N-terminated edge, both interfacing with monoatomic Ni steps. Notably, even when the initial configuration was set to AA' stacking, the N-terminated model relaxed into an AB-stacked configuration, exhibiting a binding energy approximately 3 eV/nm lower than that of B-terminated AA'-stacked structure (Figure 3i).

16136829, 0, Downloaded from https://onlinelibrary.wiley.com/doi/10.1002/smll.202513245 by Ulsan National Institute Of, Wiley Online Library on [02/04/2026]. See the Terms and Conditions (https://onlinelibrary.wiley.com/terms-and-conditions) on Wiley Online Library for rules of use; OA articles are governed by the applicable Creative Commons License

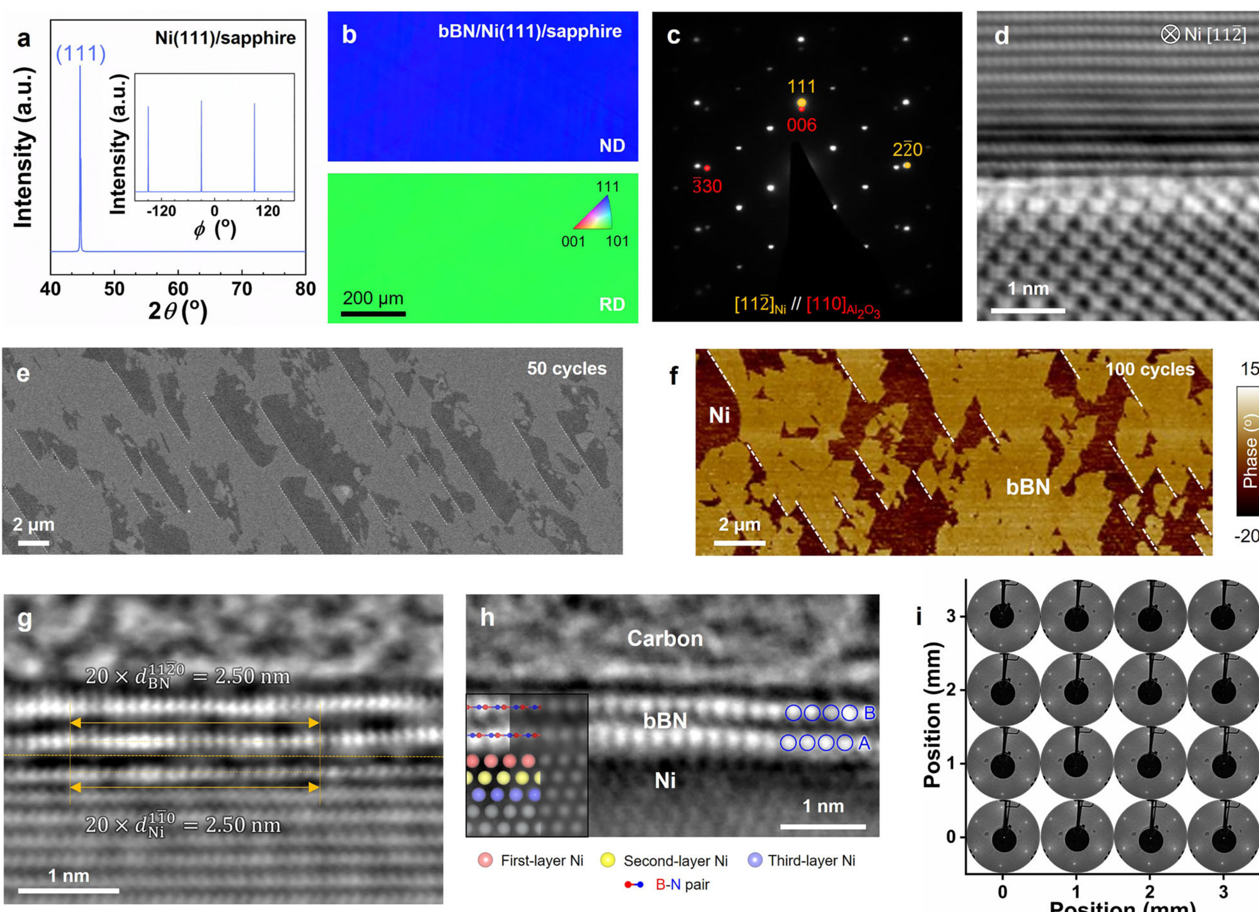

FIGURE 2 | Structural characterization of epitaxial bBN films on Ni(111). (a) XRD pattern obtained by a 2θ scan of the Ni(111) film. Inset: in-plane Φ scan of the Ni <200> direction. (b) EBSD inverse-pole figure maps of the single-crystal Ni(111) film after bBN growth. ND, normal direction. RD, rolling direction. (c, d) SAED pattern (c) and cross-sectional iDPC-STEM image (d) of the Ni/α-Al_2O_3 interface along the $[11\bar{2}]_{Ni}$ zone axis. (e) SEM image showing unidirectionally aligned bBN domains on the Ni(111) film after 50 pulse cycles. (f) AFM phase image of bBN domains after 100 pulse cycles. bBN domains are aligned with Ni steps; white dashed lines in (e, f) indicate step directions. (g, h) Cross-sectional iDPC-STEM images of bilayer bBN on Ni(111) viewed along the $[11\bar{2}]_{Ni}$ (g) and $[1\bar{1}0]_{Ni}$ (h) zone axes. Inset in (h): atomic model and corresponding simulated STEM image of the bBN–Ni (111) interface. Blue circles indicate AB-stacked bilayer BN. i) LEED patterns of the single-crystal bBN film on Ni(111), recorded over a 4 mm × 4 mm area with a 1 mm beam size.

Beyond the stacking sequence, the number of nucleation layers was also influenced by the Ni step configuration. To examine the effect of step height on multilayer nucleation, we simulated the docking of bBN nanoribbons onto Ni steps with monoatomic and triatomic heights (Figure 3j,k). When the step height was three atomic layers, thicker bBN nucleation became energetically favored. In contrast, monoatomic steps promoted bilayer formation, exhibiting an energy advantage of ~1.4 eV/nm over thicker configurations. Consistent with these predictions, thickness analysis of transferred bBN films revealed that most domains were bilayer, supporting the conclusion that monoatomic Ni steps facilitate the stable and uniform nucleation of Bernal-stacked bilayer BN in our growth system.

2.4 | Spatially Uniform Enhancement of 2D Device Performance With bBN Interlayer

Using single-crystal BN films as an interlayer between a 2D channel and a high-κ dielectric reduces charge trapping and ensures robust dielectric isolation, owing to their insulating nature and high crystalline quality. These characteristics suppress interface scattering and enhance channel performance in 2D FET devices. However, most previous studies on wafer-scale hBN growth evaluated only a limited number of devices, lacking statistical validation of hBN's wafer-scale impact (Table S2). In contrast, employing MOCVD-grown bBN as an interlayer in top-gate MoS_2 FETs demonstrated statistically significant suppression of interface scattering.

We fabricated 8 × 8 top-gate MoS_2 transistor arrays incorporating this hybrid dielectric and compared their performance against reference devices using conventional 3D dielectrics (Figure 4a,b; Figure S31). Monolayer polycrystalline MoS_2 grown by pulse-mode MOCVD served as the channel material [55]. Transfer characteristics revealed that devices with bBN interlayers exhibited improved yield, suppressed gate leakage, and reduced defect-related variability (Figure 4c; Figure S32, and Note S2 for calculation details). Despite a slightly higher equivalent oxide thickness (EOT) (3.76 nm) caused by the vdW gap and low

16136829, 0, Downloaded from https://onlinelibrary.wiley.com/doi/10.1002/smll.202513245 by Ulsan National Institute Of, Wiley Online Library on [02/04/2026]. See the Terms and Conditions (https://onlinelibrary.wiley.com/terms-and-conditions) on Wiley Online Library for rules of use; OA articles are governed by the applicable Creative Commons License

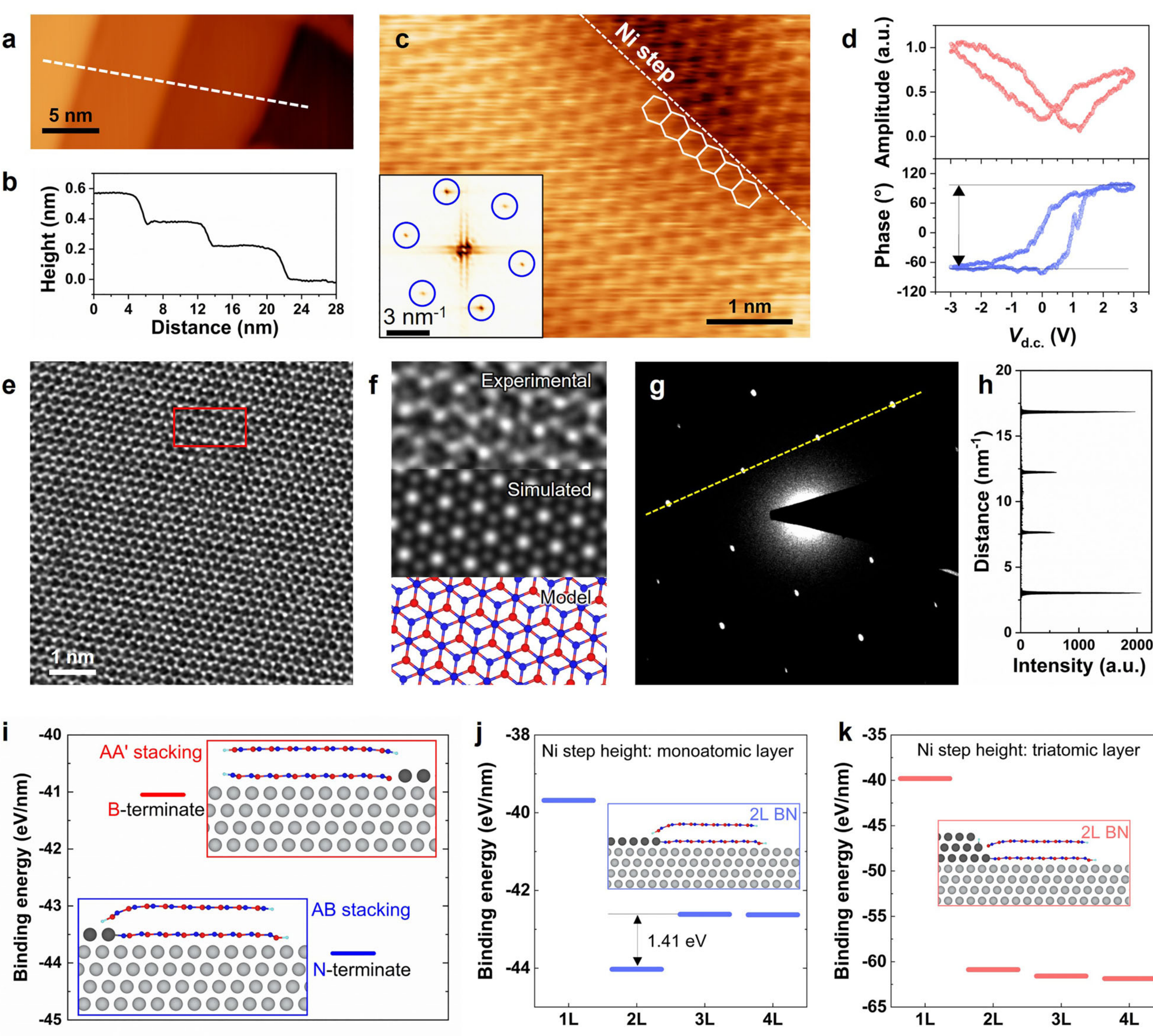

FIGURE 3 | Ni step-edge-guided nucleation mechanism of bilayer bBN. (a) STM image of the Ni(111) surface showing step edges. (b) Height profile along the white dashed line in (a), indicating monoatomic step heights. (c) Atomic-resolution STM image of bBN on Ni(111), with the step edge marked by a dashed line. Inset: corresponding FFT pattern. (d) PFM measurement of bilayer bBN on Ni(111) under an a.c. bias of 1.5 V applied during on-field mode. (e) High-resolution TEM image of a bilayer bBN film. (f) Magnified view of the red-boxed region in (e), with corresponding simulated image and structural model of Bernal-stacked bilayer BN. (g) SAED pattern of a partially grown bBN film (100 pulse cycles). (h) Intensity profile along the yellow dashed line in (g). (i) Binding energies of bilayer bBN nanoribbons at Ni monoatomic steps, comparing B-terminated and N-terminated configurations. (j, k) Binding energy variation with bBN thickness (1L–4L) at Ni step edges with (j) monoatomic and (k) triatomic step heights. Insets in (i–k) show the relaxed 2L bBN configurations for each case.

permittivity of bBN, the hybrid dielectric-integrated devices achieved superior on-state performance and stronger electrostatic control compared to 3D dielectric stacks (EOT = 2.41 nm) (Figure S33). The threshold voltage (V_{th}) of bBN-integrated devices exhibited a positive shift (2.95 ± 0.32 V *vs.* 2.01 ± 0.25 V) and reduced variation (10.7% *vs.* 12.6%), indicating that bBN interlayers suppress charge doping from amorphous oxide dielectrics (Figure 4d; Figure S34). The average on-current (I_{on}) reached 14.2 μA μm^{-1}—over fivefold higher than that of the reference device (2.5 μA μm^{-1}). To ensure a fair comparison, I_{on} was extracted at a carrier density (n_s) of 10^{13} cm^{-2}. Statistical analysis of on/off ratio and subthreshold swing (SS) further highlighted the benefit of the bBN interlayer: mean I_{on}/I_{off} = 5.3 × 10^8 and SS = 238 mV dec^{-1} (Figure S35). Collectively, these enhancements demonstrate that bilayer bBN not only preserves dielectric integrity but also improves gate modulation.

2D mapping of field-effect mobility (μ_{FE}) and interface trap density (D_{it}) across the 8 × 8 array confirmed the spatial uniformity of device performance (Figure 4e; Figure S36). The average μ_{FE} of devices incorporating bBN was 5.5 cm^2 V^{-1} s^{-1}, nine times higher than that of devices without bBN (0.61 cm^2 V^{-1} s^{-1}). The corresponding D_{it} (1.65 × 10^{13} cm^{-2} eV^{-1}) was less than half that of the reference stack, indicating that the crystalline AB-stacked BN interlayer effectively suppresses interface scattering and dielectric-induced defects.

16136829, 0, Downloaded from https://onlinelibrary.wiley.com/doi/10.1002/smll.202513245 by Ulsan National Institute Of, Wiley Online Library on [02/04/2026]. See the Terms and Conditions (https://onlinelibrary.wiley.com/terms-and-conditions) on Wiley Online Library for rules of use; OA articles are governed by the applicable Creative Commons License

16136829, 0, Downloaded from https://onlinelibrary.wiley.com/doi/10.1002/smll.202513245 by Ulsan National Institute Of, Wiley Online Library on [02/04/2026]. See the Terms and Conditions (https://onlinelibrary.wiley.com/terms-and-conditions) on Wiley Online Library for rules of use; OA articles are governed by the applicable Creative Commons License

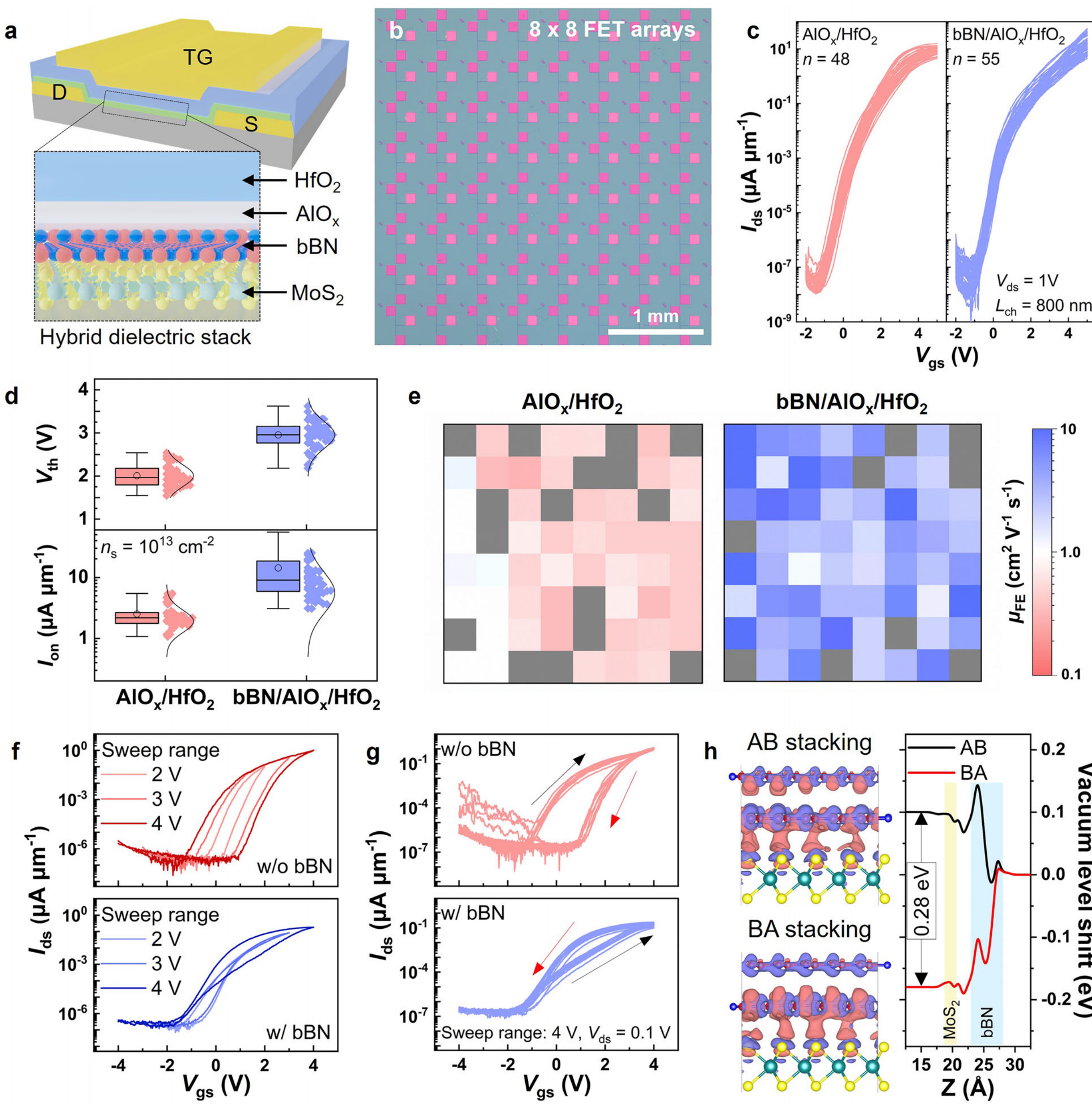

FIGURE 4 | Electrical performance of MoS_2 FET arrays with bBN interlayers. (a) Schematic describing a top-gate MoS_2 FET device integrated with hybrid dielectric stack in terms of the bBN interlayer, AlO_x buffer layer, and high-κ HfO_2 dielectric. (b) Optical image of 8 × 8 arrays of MoS_2 FETs integrated with hybrid dielectric. (c) Transfer curves (I_{ds}–V_{gs}) of FETs with AlO_x/HfO_2 (pink) and bBN/AlO_x/HfO_2 (sky-blue) dielectrics. (d) Box-and-whisker plots with normal (upper) and lognormal (lower) fitting of V_{th} and I_{on} values with different dielectric stacks. (e) Color maps of field-effect mobility, μ_{FE} extracted from transfer curves (c) in FET devices made without bBN (left) and with bBN (right). The gray position represents the failed device with gate leakage greater than 10^{-7} A at a gate bias of 1 V. (f, g) Polarization-switching-induced transfer characteristics of top-gated MoS_2 FETs without (upper) and with (lower) a bBN interlayer under various sweep ranges (f) and at a sweep range of 4 V (g). All measurements were performed at V_{ds} = 0.1 V. (h) Stacking-dependent charge redistribution in bilayer bBN/MoS_2 heterostructures: differential charge distribution mapping (left) and extracted vacuum-level shifts for AB and BA stacking configurations.

2.5 | Polarization Switching of bBN for 2D Electronic Applications

As confirmed by the PFM signals of bBN films (Figure 3d), top-gate MoS_2 FETs with bBN interlayers also exhibited ferroelectric switching, evidenced by a hysteresis loop that changed from clockwise to counterclockwise depending on the applied electric field (Figure 4f,g; Figure S37) [56]. In contrast, devices without a bBN interlayer displayed only clockwise hysteresis, with the hysteresis window widening as the sweep range increased from 2 to 4 V [57]. By comparison, devices with bBN interlayers exhibited clockwise hysteresis at sweep ranges of 1–3 V, but reversed to counterclockwise at 4 V.

To elucidate this behavior, DFT calculations were performed, confirming that the shift in the MoS_2 vacuum level induced by bBN polarization switching aligns with the transfer characteristics of the FET (Figure 4h; Figures S38–S40, and Note S3). When the stacking configuration changes from AB to BA, the bBN polarization points downward, causing a downward shift in the MoS_2 vacuum level and a relative increase in its Fermi level [19]. Consistently, in MoS_2 FETs with bBN interlayers, the threshold voltage shifted negatively during the backward sweep following switching. This confirms that the potential shift in MoS_2 due to the bBN polarization switching, as predicted by DFT, directly corresponds to the dual-sweep transfer characteristics of the devices.

3 | Conclusion

We report the first wafer-scale growth of single-crystal Bernal-stacked bilayer BN, achieved through a flow-modulated MOCVD approach combined with monoatomic step-edge-directed epitaxy on Ni(111)/sapphire substrates. This method enables self-limited bilayer nucleation and deterministic AB stacking by leveraging Ni step-edge templating, which ensures control over both stacking sequence and layer-number uniformity. The resulting bBN films exhibit high crystalline quality, atomically clean interfaces, and wafer-scale thickness uniformity, as confirmed by atomic-resolution imaging and diffraction analyses. When integrated as interlayers in MoS_2 transistor arrays, the bBN yielded spatially uniform and statistically consistent enhancements in charge transport and electrostatic gate control across all devices, owing to suppressed interface scattering at the MoS_2/bBN interface. Furthermore, the AB-stacked bBN imparted a robust ferroelectric switching functionality in top-gate 2D FETs, enabling nonvolatile polarization control of the MoS_2 channel. Collectively, these findings establish a reliable stacking-controlled route for wafer-scale bilayer BN synthesis and integration, and highlight its general applicability to scalable 2D nanoelectronics.

4 | Experimental Section

4.1 | Deposition of Ni(111) Film on Sapphire

The as-received two-inch epi-ready *c*-plane sapphire wafers with a nominal miscut of 0.2° toward the *m* axis were annealed at 1000°C for 4 h in an air atmosphere. The as-annealed sapphire wafers were cleaned by a piranha solution at 120°C for 15 min, and then rinsed in a DI water bath for 20 min. A 600-nm-thick Ni thin film was deposited on the as-prepared sapphire wafer at 550°C for 20 min using direct current sputtering equipment (SRN-120, SORONA).

4.2 | Growth of Single-Crystal bBN via MOCVD

bBN growth was performed in an MOCVD system equipped with a showerhead-type vertical cold-wall reactor with an automatic run/vent manifold system. TEB was used as the B precursor, and NH_3 was used as the N source with a H_2 carrier gas. Before bBN growth, the two-inch Ni/sapphire placed on the SiC-coated susceptor was annealed at 1100°C for 30 min in a H_2 atmosphere with a pressure of 500 Torr. The bBN growth step was initiated by reducing the pressure to 100 Torr, while maintaining the temperature. The TEB was introduced at a molar flow rate of 15 µmol/min, and the NH_3 was introduced at 2 slm. The growth cycle comprises four steps: 1) TEB injection (6 s), 2) interruption (2 s), 3) NH_3 injection (10 s), and 4) interruption (2 s). The interruption step involves the injection of only H_2 carrier gas, without the addition of TEB or NH_3. After 200 pulse cycles, complete growth of the bBN film on Ni was achieved. The cooling process was then conducted at a cooling rate of 150°C min^{-1} in a H_2/NH_3 atmosphere (Table S1), which serves to suppress the formation of the N vacancy.

4.3 | Transfer of bBN Films

The as-grown bilayer bBN film was transferred from the Ni (111) substrate via an electrochemical bubbling process [21]. A polymethyl-methacrylate (PMMA) layer was spin-coated on the bBN film. The PMMA film at the working electrode area and the edge of the wafer were removed using a laser blade. A conductive polymer-coated Cu foil was attached as the cathode. Then, TRT was attached to the PMMA-coated wafer to prevent unwanted folds during the transfer process. The transfer was carried out in a 1 M NaOH solution using a Pt wire as the anode under an applied voltage of 3 V. H_2 bubbles generated at the Ni surface facilitated the delamination of the bBN layer from the Ni substrate. To remove residual NaOH, the delaminated film was soaked in three separate DI baths for 30 min each. Following air-drying for 1 h, the samples were transferred onto the target substrate. The TRT was detached by heating at 120°C, and the PMMA layer was eliminated by dipping the sample in an acetone bath overnight. After isopropyl alcohol (IPA) rinsing and N_2 blowing, the bBN film on the target substrate was obtained through UHV annealing in a N_2/H_2 mixture at 350°C for 2 h.

4.4 | Characterizations

Surface morphologies of bBN grown on Ni(111)/sapphire were examined using cold field-emission SEM (SU8220, Hitachi) and AFM (Dimension Icon, Bruker). Raman spectra were collected with a confocal Raman microscope (alpha300R, WITec, 532 nm excitation), and optical images were obtained using an Axio Scope A1 (ZEISS). UV–vis spectra were measured with a Cary 5000 spectrophotometer (Agilent). Electrical measurements of bBN/Ni(111) were performed using conductive AFM (XE-40 and NX20, Park Systems) in contact mode with a Pt-coated tip (see Supplementary Note 4 for the details, Supporting Information). PFM data were collected in on-field mode (XE-40) using conductive tips (NSC18-CrAu, Park Systems). XPS spectra of bBN and sapphire were acquired using a monochromatic Al Kα source (ESCALAB 250Xi, Thermo Fisher). Crystallinity of Ni(111) films was assessed by EBSD (Quanta 3D FEG, FEI), θ–2θ XRD (D8 DISCOVERY, Bruker), and azimuthal XRD (X'Pert MPD, Philips). Cross-sectional STEM specimens were prepared by focused ion beam (Quanta 3D FEG, FEI), and HAADF/iDPC-STEM imaging and SAED were conducted using an aberration-corrected Titan G2 60–300 (FEI) at 200 kV. In-plane high-resolution TEM and SAED were carried out at 80 kV. Simulated STEM images were generated using the Tempas software. STM/STS experiments

16136829, 0, Downloaded from https://onlinelibrary.wiley.com/doi/10.1002/smll.202513245 by Ulsan National Institute Of, Wiley Online Library on [02/04/2026]. See the Terms and Conditions (https://onlinelibrary.wiley.com/terms-and-conditions) on Wiley Online Library for rules of use; OA articles are governed by the applicable Creative Commons License

were performed at 77 K using a UHV low-temperature STM (SPECS) under a base pressure below 5.0×10^{-11} Torr, after annealing bBN/Ni(111)/sapphire at 400°C for 4 h. LEED patterns were obtained using a ErLEED 150 system (SPECS) under a base pressure below 3.0×10^{-10} Torr, following e-beam heating at 300°C for 2 h and cooling to room temperature.

4.5 | Top-Gate FET Fabrication and Electrical Measurement

A bottom-contact structure was employed to ensure uniform device geometry in polycrystalline MoS_2 FETs. Electrode patterns with 800 nm channel lengths were defined via laser lithography (MicroWriter ML3), followed by Ti/Au (3/12 nm) deposition and lift-off. The electrodes underwent O_2 ashing at 300°C for 5 min to remove resist residues. A monolayer MoS_2 film was synthesized on an 8-inch SiO_2/Si wafer via pulse-mode MOCVD [44]. The PMMA/TRT-assisted transfer method was used to transfer MoS_2 onto the bottom-contact patterned substrate, followed by PMMA removal with hot acetone and UHV annealing at 200°C for 2 h to improve adhesion. The MoS_2 channel was patterned using laser lithography and O_2 ashing. A bilayer bBN film was transferred onto the MoS_2 using an electrochemical bubbling method. Because uniform deposition of a nanometer-scale high-κ dielectric layer on bBN is hindered by its inert and hydrophobic surface with low precursor adsorption during atomic layer deposition (ALD) [23], an ultrathin Al seed layer was introduced prior to HfO_2 deposition. A 1.5 nm-thick Al seed layer was e-beam evaporated, followed by 6 nm HfO_2 deposition via ALD at 200°C, forming a pinhole-free bBN/AlO_x/HfO_2 hybrid dielectric stack (Figure S41). The top-gate electrode (Ti/Au, 3/15 nm) was deposited, and a via was opened by BCl_3-based dry etching to expose the bottom-contact pads. Electrical measurements were performed in high vacuum (~10^{-5} Torr) at room temperature using a cryogenic probe station (Lakeshore CRX-4K) and a Keithley 4200-SCS analyzer.

4.6 | DFT Calculations of bBN Formation

The DFT calculations of binding energy for various BN–Ni (111) configurations were conducted using Quantum Atomistic-ToolKit (ATK) tool version V-2023.12 (Synopsys). The exchange-correlation potential was described by the Perdew-Burke-Ernzerhof (PBE) in the generalized gradient approximation (GGA). Gimme DFT-D3 method was activated as a vdW correction. A Monkhorst-Pack k-point grid of $1 \times 11 \times 1$ was applied for the bBN nanoribbon on the Ni (111) surface with atomic step layers with an energy cutoff of 85 Hartree. A vacuum slab of 30 Å was used to avoid interactions between adjacent cells in the vertical direction. To reduce spurious interactions when forming supercells in a slab model with a vicinal Ni surface, the distance between the bBN nanoribbon and the undocked step edge was set to a minimum of 10 Å. The structural optimization was performed until the energy and force variations were reduced to 1×10^{-5} eV and 0.01 eV/Å, respectively. To isolate the effect of the interface configuration without introducing strain, the Ni atoms were fixed during structural relaxation, and the lattice constant was set to 2.512 Å to match that of the BN crystal. The binding energy for the BN structures on the Ni (111) slab was calculated as follows:

$$E_b = E_{BN} + E_{Ni} - E_{BN-Ni} \quad (1)$$

where E_{BN}, E_{Ni}, and $E_{BN\text{-}Ni}$ are the energies of free-standing BN, the Ni slab, and the BN structure on the Ni slab, respectively. For the BN nanoribbon system with Ni steps, the binding energy was normalized with respect to the length along the Ni step direction. The initial atomic configuration of the first BN layer in all BN nanostructures was adopted from the most stable configuration obtained in the monolayer hBN nanoribbon calculation (Figure S42).

Author Contributions

Jaewon Wang and Soon-Yong Kwon conceived the idea and designed the experiments; Jaewon Wang, Hyeonwoo Lee, and Haeng Un Yeo performed the epitaxial growth of single-crystal bBN films on Ni(111)/sapphire; Jaewon Wang performed the material characterizations with assistance from Hyeonwoo Lee, Haeng Un Yeo, Sora Jang, Ju-Hyoung Han, Juwon Han, Jaeeun Park, and Young Ho Jin; Hyeonwoo Lee, and Changwook Jeong performed DFT calculations; Jaemin Kim and Zonghoon Lee performed (S)TEM characterizations; Cheol Hwan Yoon, Junseop Noh, Huijun Han, and Hyung-Joon Shin performed STM, CAFM and PFM measurements; Chanyong Hwang provided LEED measurements; Min Seok Yoo and Minsu Seol provided the polycrystalline MoS_2 films; Kitae Park and Tae-Sik Yoon provided guidance for atomic layer deposited high-κ dielectric layer; Joonki Suh provided a platform for MoS_2 characterizations; Jaewon Wang, Sora Jang and Seunguk Song designed the FET structures; Jaewon Wang performed the device fabrication and electrical measurements of the MoS_2 FET arrays; Jaewon Wang and Soon-Yong Kwon wrote the manuscript with input from all authors; All authors contributed to the analysis and discussion of the results leading to the manuscript; Soon-Yong Kwon planned and supervised the project.

Acknowledgements

This work was supported by the Basic Science Research Program (Grant Nos. 2021R1A2C2094674, RS-2023-00257666), Basic Research Laboratory Program (Grant No. RS-2023-00218908), and Nano & Material Technology Development Program (Grant No. RS-2024-00408180) through the National Research Foundation (NRF) of Korea funded by the Ministry of Science and ICT, the HRD Program for Industrial Innovation (Grant No. P0023703) and the Technology Innovation Program (Grant No. RS-2023-00231956) through the Korea Government (MOTIE) funded by Korea Institute for Advancement of Technology (KIAT), the Research Fund (Grant No. IO250114-11738-02) of Samsung-UNIST Semiconductor Cluster funded by Samsung Electronics, the Samsung Research Funcding & Incubation Center for Future Technology (SRFC-IT2502-01), the Research Fund (IBS-R019-G1) of Institute of Basic Science, and the Research Fund (Grant Nos. 1.260003.01 & 1.230063.01) of UNIST. This work has benefited from the use of the facilities at UNIST Office of Research Facilities and Training (ResFacT) Central Research Facilities.

Funding

This work was supported by the Basic Science Research Program (Grant Nos. 2021R1A2C2094674, RS-2023-00257666), Basic Research Laboratory Program (Grant No. RS-2023-00218908), and Nano & Material Technology Development Program (Grant No. RS-2024-00408180) through the National Research Foundation (NRF) of Korea funded by the Ministry of Science and ICT, the HRD Program for Industrial Innovation (Grant No. P0023703) and the Technology Innovation Program (Grant No. RS-2023-00231956) through the Korea Government (MOTIE) funded by Korea Institute for Advancement of Technology (KIAT), the Research Fund

16136829, 0, Downloaded from https://onlinelibrary.wiley.com/doi/10.1002/smll.202513245 by Ulsan National Institute Of, Wiley Online Library on [02/04/2026]. See the Terms and Conditions (https://onlinelibrary.wiley.com/terms-and-conditions) on Wiley Online Library for rules of use; OA articles are governed by the applicable Creative Commons License

(Grant No. IO250114-11738-02) of Samsung-UNIST Semiconductor Cluster funded by Samsung Electronics, the Samsung Research Funding & Incubation Center for Future Technology (SRFC-IT2502-01), the Research Fund (IBS-R019-G1) of Institute of Basic Science, and the Research Fund (Grant Nos. 1.260003.01 & 1.230063.01) of UNIST.

Conflicts of Interest

The authors declare no conflicts of interest.

Data Availability Statement

The data that support the findings of this study are available from the corresponding author upon reasonable request.

References

1. S. Moon, J. Kim, J. Park, et al., "Hexagonal Boron Nitride for Next-Generation Photonics and Electronics," *Advanced Materials* 35 (2023): 2204161, https://doi.org/10.1002/adma.202204161.

2. S. Roy, X. Zhang, A. B. Puthirath, et al., "Structure, Properties and Applications of Two-Dimensional Hexagonal Boron Nitride," *Advanced Materials* 33 (2021): 2101589, https://doi.org/10.1002/adma.202101589.

3. L. Du, T. Hasan, A. Castellanos-Gomez, et al., "Engineering Symmetry Breaking in 2D Layered Materials," *Nature Reviews Physics* 3 (2021): 193–206, https://doi.org/10.1038/s42254-020-00276-0.

4. Y. Liu, X. Duan, H.-J. Shin, S. Park, Y. Huang, and X. Duan, "Promises and Prospects of Two-Dimensional Transistors," *Nature* 591 (2021): 43–53, https://doi.org/10.1038/s41586-021-03339-z.

5. C. Liu, H. Chen, S. Wang, et al., "Two-Dimensional Materials for Next-Generation Computing Technologies," *Nature Nanotechnology* 15 (2020): 545–557, https://doi.org/10.1038/s41565-020-0724-3.

6. Y. Y. Illarionov, T. Knobloch, M. Jech, et al., "Insulators for 2D Nanoelectronics: The Gap to Bridge," *Nature Communications* 11 (2020): 3385, https://doi.org/10.1038/s41467-020-16640-8.

7. A. E. Naclerio and P. R. Kidambi, "A Review of Scalable Hexagonal Boron Nitride (h -BN) Synthesis for Present and Future Applications," *Advanced Materials* 35 (2023): 2207374, https://doi.org/10.1002/adma.202207374.

8. C. R. Dean, A. F. Young, I. Meric, et al., "Boron Nitride Substrates for High-Quality Graphene Electronics," *Nature Nanotechnology* 5 (2010): 722–726, https://doi.org/10.1038/nnano.2010.172.

9. K. K. Kim, A. Hsu, X. Jia, et al., "Synthesis of Monolayer Hexagonal Boron Nitride on Cu Foil Using Chemical Vapor Deposition," *Nano Letters* 12 (2012): 161–166, https://doi.org/10.1021/nl203249a.

10. L. Wang, J. Qi, W. Wei, et al., "Bevel-Edge Epitaxy of Ferroelectric Rhombohedral Boron Nitride Single Crystal," *Nature* 629 (2024): 74–79, https://doi.org/10.1038/s41586-024-07286-3.

11. J. Qi, C. Ma, Q. Guo, et al., "Stacking-Controlled Growth of rBN Crystalline Films With High Nonlinear Optical Conversion Efficiency up to 1%," *Advanced Materials* 36 (2024): 2303122, https://doi.org/10.1002/adma.202303122.

12. S.-S. Wong, Z.-Y. Lin, S.-Z. Ho, et al., "Epitaxial Ferroelectric Hexagonal Boron Nitride Grown on Graphene," *Advanced Materials* 37 (2025): 2414442, https://doi.org/10.1002/adma.202414442.

13. K. Yasuda, X. Wang, K. Watanabe, T. Taniguchi, and P. Jarillo-Herrero, "Stacking-Engineered Ferroelectricity in Bilayer Boron Nitride," *Science* 372 (2021): 1458–1462, https://doi.org/10.1126/science.abd3230.

14. K. Yasuda, E. Zalys-Geller, X. Wang, et al., "Ultrafast High-Endurance Memory Based on Sliding Ferroelectrics," *Science* 385 (2024): 53–56, https://doi.org/10.1126/science.adp3575.

15. X.-J. Zhao, Y. Yang, D.-B. Zhang, and S.-H. Wei, "Formation of Bloch Flat Bands in Polar Twisted Bilayers Without Magic Angles," *Physical Review Letters* 124 (2020): 086401, https://doi.org/10.1103/PhysRevLett.124.086401.

16. H. Ochoa and A. Asenjo-Garcia, "Flat Bands and Chiral Optical Response of moiré Insulators," *Physical Review Letters* 125 (2020): 037402, https://doi.org/10.1103/PhysRevLett.125.037402.

17. S. L. Moore, C. J. Ciccarino, D. Halbertal, et al., "Nanoscale Lattice Dynamics in Hexagonal Boron Nitride Moiré Superlattices," *Nature Communications* 12 (2021): 5741, https://doi.org/10.1038/s41467-021-26072-7.

18. X. Wang, C. Xu, S. Aronson, et al., "Moiré Band Structure Engineering Using a Twisted Boron Nitride Substrate," *Nature Communications* 16 (2025): 178, https://doi.org/10.1038/s41467-024-55432-2.

19. M. Cho, B. Datta, K. Han, et al., "Moiré Exciton Polaron Engineering via Twisted hBN," *Nano Letters* 25 (2024): 1381–1388, https://doi.org/10.1021/acs.nanolett.4c04996.

20. D. S. Kim, C. Xiao, R. C. Dominguez, et al., "Moiré Ferroelectricity Modulates Light Emission From a Semiconductor Monolayer," *Science Advances* 11 (2025): adt7789, https://doi.org/10.1126/sciadv.adt7789.

21. T.-A. Chen, C.-P. Chuu, C.-C. Tseng, et al., "Wafer-Scale Single-Crystal Hexagonal Boron Nitride Monolayers on Cu (111)," *Nature* 579 (2020): 219–223, https://doi.org/10.1038/s41586-020-2009-2.

22. K. Y. Ma, L. Zhang, S. Jin, et al., "Epitaxial Single-Crystal Hexagonal Boron Nitride Multilayers on Ni (111)," *Nature* 606 (2022): 88–93, https://doi.org/10.1038/s41586-022-04745-7.

23. Y. Wang, C. Zhao, X. Gao, et al., "Ultraflat Single-Crystal Hexagonal Boron Nitride for Wafer-Scale Integration of a 2D-Compatible High-κ Metal Gate," *Nature Materials* 23 (2024): 1495–1501, https://doi.org/10.1038/s41563-024-01968-z.

24. J. Meng, X. Zhang, Y. Wang, et al., "Aligned Growth of Millimeter-Size Hexagonal Boron Nitride Single-Crystal Domains on Epitaxial Nickel Thin Film," *Small* 13 (2017): 1604179, https://doi.org/10.1002/smll.201604179.

25. J. Meng, B. Ming, X. Zhang, et al., "Controlled Growth of Unidirectionally Aligned Hexagonal Boron Nitride Domains on Single Crystal Ni (111)/MgO Thin Films," *Crystal Growth & Design* 19 (2018): 453–459, https://doi.org/10.1021/acs.cgd.8b01542.

26. C. Liu, T. Liu, Z. Zhang, et al., "Understanding Epitaxial Growth of Two-Dimensional Materials and Their Homostructures," *Nature Nanotechnology* 19 (2024): 907–918, https://doi.org/10.1038/s41565-024-01704-3.

27. L. Britnell, R. V. Gorbachev, R. Jalil, et al., "Electron Tunneling Through Ultrathin Boron Nitride Crystalline Barriers," *Nano Letters* 12 (2012): 1707–1710, https://doi.org/10.1021/nl3002205.

28. L. H. Li, E. J. G. Santos, T. Xing, et al., "Dielectric Screening in Atomically Thin Boron Nitride Nanosheets," *Nano Letters* 15 (2015): 218–223, https://doi.org/10.1021/nl503411a.

29. M. Maruyama and S. Okada, "Effect of Interlayer Stacking Arrangement on the Dielectric Properties of Hexagonal Boron Nitride Thin Films," *FlatChem* 48 (2024): 100751, https://doi.org/10.1016/j.flatc.2024.100751.

30. S. Fukamachi, P. Solís-Fernández, K. Kawahara, et al., "Large-Area Synthesis and Transfer of Multilayer Hexagonal Boron Nitride for Enhanced Graphene Device Arrays," *Nature Electronics* 6 (2023): 126–136, https://doi.org/10.1038/s41928-022-00911-x.

31. Y. Shi, C. Hamsen, X. Jia, et al., "Synthesis of Few-Layer Hexagonal Boron Nitride Thin Film by Chemical Vapor Deposition," *Nano Letters* 10 (2010): 4134–4139, https://doi.org/10.1021/nl1023707.

32. S. M. Kim, A. Hsu, M. H. Park, et al., "Synthesis of Large-area Multilayer Hexagonal Boron Nitride for High Material Performance," *Nature Communications* 6 (2015): 8662, https://doi.org/10.1038/ncomms9662.

33. Y. Uchida, S. Nakandakari, K. Kawahara, S. Yamasaki, M. Mitsuhara, and H. Ago, "Controlled Growth of Large-Area Uniform Multilayer Hexagonal Boron Nitride as an Effective 2D Substrate," *ACS Nano* 12 (2018): 6236–6244, https://doi.org/10.1021/acsnano.8b03055.

16136829, 0, Downloaded from https://onlinelibrary.wiley.com/doi/10.1002/smll.202513245 by Ulsan National Institute Of, Wiley Online Library on [02/04/2026]. See the Terms and Conditions (https://onlinelibrary.wiley.com/terms-and-conditions) on Wiley Online Library for rules of use; OA articles are governed by the applicable Creative Commons License

34. J. S. Lee, S. H. Choi, S. J. Yun, et al., "Wafer-scale Single-Crystal Hexagonal Boron Nitride Film via Self-Collimated Grain Formation," *Science* 362 (2018): 817–821, https://doi.org/10.1126/science.aau2132.

35. L. Wang, X. Xu, L. Zhang, et al., "Epitaxial Growth of a 100-Square-Centimetre Single-Crystal Hexagonal Boron Nitride Monolayer on Copper," *Nature* 570 (2019): 91–95, https://doi.org/10.1038/s41586-019-1226-z.

36. G. Lu, T. Wu, Q. Yuan, et al., "Synthesis of Large Single-Crystal Hexagonal Boron Nitride Grains on Cu–Ni Alloy," *Nature Communications* 6 (2015): 6160, https://doi.org/10.1038/ncomms7160.

37. Y. Stehle, H. M. Meyer, R. R. Unocic, et al., "Synthesis of Hexagonal Boron Nitride Monolayer: Control of Nucleation and Crystal Morphology," *Chemistry of Materials* 27 (2015): 8041–8047, https://doi.org/10.1021/acs.chemmater.5b03607.

38. S. Y. Kim, J. Kwak, C. V. Ciobanu, and S.-Y. Kwon, "Recent Developments in Controlled Vapor-Phase Growth of 2D Group 6 Transition Metal Dichalcogenides," *Advanced Materials* 31 (2019): 1804939, https://doi.org/10.1002/adma.201804939.

39. D. H. Lee, Y. Sim, J. Wang, and S.-Y. Kwon, "Metal–Organic Chemical Vapor Deposition of 2D van der Waals Materials—The Challenges and the Extensive Future Opportunities," *APL Materials* 8 (2020): 030901, https://doi.org/10.1063/1.5142601.

40. Y. Kobayashi and T. Makimoto, "Growth of Boron Nitride on 6H–SiC Substrate by Flow-Rate Modulation Epitaxy," *Japanese Journal of Applied Physics* 45 (2006): 3519, https://doi.org/10.1143/Jjap.45.3519.

41. A. Rice, A. Allerman, M. Crawford, et al., "Effects of Deposition Temperature and Ammonia Flow on Metal-Organic Chemical Vapor Deposition of Hexagonal Boron Nitride," *Journal of Crystal Growth* 485 (2018): 90–95, https://doi.org/10.1016/j.jcrysgro.2017.12.011.

42. A. Ismach, H. Chou, D. A. Ferrer, et al., "Toward the Controlled Synthesis of Hexagonal Boron Nitride Films," *ACS Nano* 6 (2012): 6378–6385, https://doi.org/10.1021/nn301940k.

43. J. Kwak, S.-Y. Kim, Y. Jo, et al., "Unraveling the Water Impermeability Discrepancy in CVD-Grown Graphene," *Advanced Materials* 30 (2018): 1800022, https://doi.org/10.1002/adma.201800022.

44. Q. Cai, D. Scullion, A. Falin, et al., "Raman Signature and Phonon Dispersion of Atomically Thin Boron Nitride," *Nanoscale* 9 (2017): 3059–3067, https://doi.org/10.1039/c6nr09312d.

45. Y. Yuan, J. Weber, J. Li, et al., "On the Quality of Commercial Chemical Vapour Deposited Hexagonal Boron Nitride," *Nature Communications* 15 (2024): 4518, https://doi.org/10.1038/s41467-024-48485-w.

46. J. Li, A. Samad, Y. Yuan, et al., "Single-Crystal hBN Monolayers From Aligned Hexagonal Islands," *Nature Communications* 15 (2024): 8589, https://doi.org/10.1038/s41467-024-52944-9.

47. F. Zeng, R. Wang, W. Wei, et al., "Stamped Production of Single-Crystal Hexagonal Boron Nitride Monolayers on Various Insulating Substrates," *Nature Communications* 14 (2023): 6421, https://doi.org/10.1038/s41467-023-42270-x.

48. Y. Hu, J. Peng, M. Pan, et al., "Wafer-Scale Epitaxial Single-Crystalline Ni (111) Films on Sapphires for Graphene Growth," *Journal of Materials Science* 56 (2021): 3220–3229, https://doi.org/10.1007/s10853-020-05450-4.

49. J. Kwak, J. H. Chu, J.-K. Choi, et al., "Near Room-Temperature Synthesis of Transfer-Free Graphene Films," *Nature Communications* 3 (2012): 645, https://doi.org/10.1038/ncomms1650.

50. D. Wickramaratne, L. Weston, and C. G. Van de Walle, "Monolayer to Bulk Properties of Hexagonal Boron Nitride," *The Journal of Physical Chemistry C* 122 (2018): 25524–25529, https://doi.org/10.1021/acs.jpcc.8b09087.

51. L. Liu, J. Park, D. A. Siegel, et al., "Heteroepitaxial Growth of Two-Dimensional Hexagonal Boron Nitride Templated by Graphene Edges," *Science* 343 (2014): 163–167, https://doi.org/10.1126/science.1246137.

52. Q. Zhang, Y. Chen, C. Zhang, et al., "Bandgap Renormalization and Work Function Tuning in $MoSe_2$/hBN/Ru (0001) Heterostructures," *Nature Communications* 7 (2016): 13843, https://doi.org/10.1038/ncomms13843.

53. S. M. Gilbert, T. Pham, M. Dogan, et al., "Alternative Stacking Sequences in Hexagonal Boron Nitride," *2D Materials* 6 (2019): 021006, https://doi.org/10.1088/2053-1583/ab0e24.

54. H. J. Park, J. Cha, M. Choi, et al., "One-Dimensional Hexagonal Boron Nitride Conducting Channel," *Science Advances* 6 (2020): aay4958, https://doi.org/10.1126/sciadv.aay4958.

55. M. Seol, M.-H. Lee, H. Kim, et al., "High-Throughput Growth of Wafer-Scale Monolayer Transition Metal Dichalcogenide via Vertical Ostwald Ripening," *Advanced Materials* 32 (2020): 2003542, https://doi.org/10.1002/adma.202003542.

56. X. Liu, D. Wang, K.-H. Kim, et al., "Post-CMOS Compatible Aluminum Scandium Nitride/2D Channel Ferroelectric Field-Effect-Transistor Memory," *Nano Letters* 21 (2021): 3753–3761, https://doi.org/10.1021/acs.nanolett.0c05051.

57. F. Urban, F. Giubileo, A. Grillo, et al., "Gas Dependent Hysteresis in MoS_2 Field Effect Transistors," *2D Materials* 6 (2019): 045049, https://doi.org/10.1088/2053-1583/ab4020.

Supporting Information

Additional supporting information can be found online in the Supporting Information section.

Supporting File: smll73102-sup-0001-SuppMat.docx.

16136829, 0, Downloaded from https://onlinelibrary.wiley.com/doi/10.1002/smll.202513245 by Ulsan National Institute Of, Wiley Online Library on [02/04/2026]. See the Terms and Conditions (https://onlinelibrary.wiley.com/terms-and-conditions) on Wiley Online Library for rules of use; OA articles are governed by the applicable Creative Commons License